

Solvent Effects on the Self-Assembly of 1-Bromoeicosane on Graphite. Part II. Theory

Boaz Ilan,^{†,‡,§} Gina M. Florio,^{§,||} Tova L. Werblowsky,^{⊥,‡,§} Thomas Müller,^{#,‡,§}
 Mark S. Hybertsen,[∇] B. J. Berne,^{*,‡} and George W. Flynn^{*,‡,§}

Department of Chemistry, Columbia University, New York, New York 10027, Center for Electron Transport in Molecular Nanostructures, Columbia University, New York, New York 10027, Department of Chemistry and Department of Physics, St. John's University, Queens, New York 11439, and Center for Functional Nanomaterials, Brookhaven National Laboratory, Upton, New York 11973

Received: October 17, 2008; Revised Manuscript Received: December 17, 2008

The phase ordering of 1-bromoeicosane (C₂₀H₄₁Br) at the liquid-graphite and vacuum-graphite interfaces is examined through a joint experimental (part I) and theoretical effort (part II). The stable morphologies under solvent and ultrahigh vacuum conditions are revealed by STM experiments to be the head-to-head structures with 90° and 60° lamella–backbone angles, respectively. At 90° and 60° close packing is attained, independent of the corrugation of the graphite lattice. The potential energy of the minimized 60° structure is slightly lower than that of the 90° structure under vacuum conditions. In addition, the basin of the potential energy surface about the 90° form is very narrow. All-atom molecular dynamics simulations depict a 90°-to-60° phase transition in vacuum. Both morphologies are stable when an explicit solvent model is included. We speculate that the choice of the 90° form under solvent is driven by symmetry considerations and the self-assembly pathway. For example, the 90° structure may serve as a superior template for solvent capping. An implicit solvent model fails to stabilize the 90° form; however, it does lower the potential energy of this structure relative to the 60° geometry.

Introduction

Self-assembled functionalized organic molecules on surfaces display a rich variety of highly ordered and periodic morphologies.^{1,2} Clues for understanding the molecular unit cell of the self-assemblies are provided by the identity and orientation with respect to the surface of the functional groups (“Chemical Markers”) through the variation in their scanning tunneling microscope (STM)³ image contrast.^{2,4,5} Fascinating electronic structure and surface ordering phenomena such as moiré patterns, odd/even chain length effects,⁶ polymorphism,^{7,8} and chiral segregation by achiral coadsorbates⁹ have been disclosed by direct observation using STM. Molecular modeling complemented by first principles^{10–12} and classical simulations^{13–19} provides for reconstruction of the STM images as well as thermodynamic characterization of the self-assembly morphologies. Unraveling the hierarchy of driving forces for the self-assembly process, the dominant substrate–adsorbate interactions, and the subtle interaction of intramolecular geometric constraints, van der Waals (vdW) and electrostatic forces, will ultimately lead to the development of new surface patterning and lithographic strategies.

The interplay of chain packing and substrate registry has been examined extensively for the self-assembly of normal alkanes on various substrates. For example, short even- and odd-length *n*-alkanes on graphite display 60° (herringbone) and 90° lamella–backbone (LB) angle morphologies, respectively,²⁰ corresponding to the condition for which close packing is satisfied.²¹ Krishnan et al. have successfully simulated the registry (uniaxial incommensurate-to-commensurate) transition that *n*-alkanes undergo with respect to the graphite lattice upon coverage.^{18,19} Marchenko and Cousty observed 90° LB morphologies for a series of *n*-alkanes on Au(111) at chain lengths corresponding to a multiple integer of the superposition of the spacing of the gold lattice and the alkane backbone.²² For incommensurate chain lengths an increasing fraction of the surface was covered by 60° LB morphologies coexisting with the 90° form; upon annealing the 60° structure relaxed back to a 90° structure.²² Zhang et al. have observed, on the other hand, both an odd/even and a chain length effect on the stabilities of the 60° and 90° morphologies for the *n*-alkanes following surface reconstruction of Au(111).²³ The relative stability of the 90° and 60° phases for *n*-alkanes on Au(111) and MoSe₂ has been examined by calculating the potential energy as a function of the LB angle.^{14,15}

Halogen substituents partition the 90° and 60° symmetries of *n*-alkanes into head-to-head and head-to-tail patterns. The 1-haloheptane series displays a head-to-head 60° structure on highly ordered pyrolytic graphite (HOPG) under ultra high vacuum (UHV) conditions.¹⁷ 1-bromoeicosane (henceforth BrC₂₀) also displays a head-to-head 60° nonherringbone form on HOPG under UHV conditions whereas it displays, along with 1-bromodocosane (C₂₂H₄₅Br),⁴ a head-to-head 90° structure under solvent. Deposition under solvent cannot be performed for the lighter 1-haloheptanes. Long bromoalkanes appear to be unique relative to the *n*-alkanes in that coverage by solvent

* Authors to whom correspondence should be addressed. (G.W.F.) Telephone: 212-854-4162. E-mail: gwfl@columbia.edu. (B.J.B.) Telephone: 212-854-2186. E-mail: bb8@columbia.edu.

[†] Current address: Schrödinger, L.L.C., New York, NY 10036.

[‡] Department of Chemistry, Columbia University.

[§] Center for Electron Transport in Molecular Nanostructures, Columbia University.

^{||} Department of Chemistry and Department of Physics, St. John's University.

[⊥] Current address: Department of Chemistry and Physics, Touro College, New York, NY 10010.

[#] Current address: Veeco Metrology Group, 112 Robin Hill Road, Santa Barbara, CA 93117.

[∇] Center for Functional Nanomaterials, Brookhaven National Laboratory.

results in a different LB morphology. Suspecting that the solvent dielectric constant plays a role in stabilizing the head-to-head dipole moment interactions for the 90° structure, we have used STM to image BrC₂₀ under seven different solvents covering a wide range of dielectric constants and architectures. (See companion paper, part I.²⁴) None of the examined solvents manifested the 60° LB angle structure.

This paper extends previous work in our groups on the self-assembly properties of 1-haloalkanes on HOPG under vacuum.^{17,25,26} For example, in an earlier study, the potential energy of 1-bromohexane and 1-bromoheptane adsorbed on graphite at the vacuum-solid interface was broken into its various component parts, e.g., electrostatic and Lennard Jones (LJ) contributions. This approach uncovered the subtle factors governing the preference for the head-to-head 60° form over the head-to-tail 60° form, the unfavorable head-to-head dipole interactions for the 90° form¹⁷ and the formation of herringbone pattern for the odd-length 1-bromoheptane.²⁶ In the present paper, we perform potential energy surface (PES) calculations and molecular dynamics (MD) simulations of the head-to-head 60° and head-to-head 90° morphologies of BrC₂₀ on graphite under vacuum as well as at the liquid–solid interface using an explicit solvent model. We also incorporate, for the first time, a triple-dielectric implicit solvent methodology²⁷ into MD simulations of self-assembly processes on conducting surfaces. The implicit solvent model serves to isolate the dielectric contribution due to the solvent. The simulation results are compared to experimental findings presented in the companion paper.²⁴ The modeling of organic solvents is considered challenging in that they couple strongly to the ordered adsorbate layer. Many exciting and theoretically unexplored aspects of self-assembly have been studied experimentally at the liquid–solid interface (such as chirality and polymorphic hydrogen bonding networks),^{5,8,28} which suggests theoretical modeling of the type performed here.

Methods

The simulation (SIM) molecular dynamics program (H. A. Stern, H. Xu, E. Harder, F. Rittner, M. Pavese, and B.J.B., unpublished work) was used for all of the calculations described here. The all-atom optimized potentials for liquid simulations (OPLS-AA) force field^{29,30} was used for the intramolecular and intermolecular interactions of the adsorbate and solvent molecules. The all-atom representation (inclusion of hydrogen atoms) is expected to provide better modeling of chain packing and registry with the substrate than the united atom representation. The intramolecular potential energy consists of harmonic angular bending and bond stretching contributions and the torsions are modeled by a Fourier expansion in the dihedral angles. The intermolecular interactions are represented by nonpolarizable electrostatics and a standard 6–12 LJ potential to describe vdW dispersive and repulsive forces. A geometric combining rule is used for the calculation of LJ parameters for unlike atoms. The electrostatic and LJ parameters for the alkyl chains were taken from the standard OPLS-AA parameter files, whereas the halogenated functional was specially fitted by employing the triple- ξ contraction of the Los Alamos LACVP³¹ basis-set (LACV3P), Becke's 3-parameter exchange functional and Lee Yang and Parr correlation functional (B3LYP)^{32,33} within the Jaguar program³⁴ to extract more exact electrostatics for this atom. The all-atom parametrization of BrC₂₀ by Jaguar gave nearly identical values for the partial charges of the halogenated functional as was determined previously for a united-atom representation of BrC₆ by the BOSS³⁵ simulation program and parameters derived from other semiclassical fits

(CM3_AM1 and CM3_PM3).^{36,37} We have therefore applied the same partial charge¹⁷ for the Br headgroup (−0.22 e). The partial charges of the hydrogens of the headgroup are maintained at the standard OPLS-AA value of 0.06 e, and the partial charge on the carbon of the headgroup is adjusted to 0.1 e to satisfy electrical neutrality.

The interaction with the hexagonal graphite substrate is described by LJ dispersion forces represented by the Steele³⁸ potential in combination with an image charge interaction term. The latter is commonly included³⁹ to describe the effect of placing a semimetallic surface in close proximity to a set of static external charges.⁴⁰ The image plane is located at $z_{\text{graphite-image}} = d/2$ where the distance d is the graphite interlayer spacing (3.35 Å), and the convention for the z coordinate system in these types of simulations places the topmost graphite layer sheet at the $z = 0$ position. Each molecular point charge interacts with its own image and all of the other images, but the image charges do not interact with each other in this model. The Steele potential describes the graphite surface by a Fourier expansion in the graphite lattice vectors, and the substrate–adsorbate and substrate–solvent interactions through a LJ potential. The top two layers are modeled as a fully corrugated potential, and the rest of the substrate is included as a smooth potential for a total of 40 layers. The parameters used for the Steele potential ($\sigma_{\text{surface}} = 3.55$ Å, $\epsilon_{\text{surface}} = 0.07$ kcal/mol), when used with a geometric combining rule and the standard OPLS alkyl parameters, were found to closely match the previously reported values⁴¹ used to compare calculated and experimental melting temperatures of alkane monolayers on graphite surfaces.

All of the minimizations were performed by using the truncated Newton algorithm package TNPACK⁴² within SIM. Molecular dynamics in SIM were carried out for the *NVT* ensemble, by using the Nose–Hoover chains method^{43,44} for the proper equilibration of the bath temperature in the canonical ensemble. The simulations are performed without periodic boundary conditions to avoid imposing an artificial periodicity on the system, thereby obtaining an independent validation of the experimentally determined unit cell parameters for the different thermodynamic, solvent and vacuum conditions. Such a methodology has been employed by Cheng and Klein, and Krishnan and Balasubramanian for the study of melting¹³ and registry^{18,19} transitions of ethylene and *n*-hexane, respectively, on graphite. Ideally, the study of morphology transitions should be carried out by a variable box shape method.⁴⁵ The application of the Steele potential restricts, however, the lengths of the simulation box to be an integer multiple of the graphite periodicity.

The implicit solvent approach (Figure 1) is modeled by a dielectric continuum above the adsorbate layer with the image plane placed at $z_{\text{solvent-image}} = 5.8$ Å, approximately halfway between the simulated average position of the adsorbate and explicit solvent (undecanol), at $z \approx 3.5$ Å and $z \approx 7.2$ Å, respectively. The image charge interactions between the solvent and the graphite are accounted for by an extension²⁷ of the image charge method for three dielectric continuums, given by the following expression:

$$\Delta E = -\frac{e^2}{2\epsilon_v} \sum_{n=0}^{\infty} (\eta\xi)^n \left[\frac{\eta}{2Z + nd_{SG}} + \frac{\xi}{-2Z + nd_{SG}} + \frac{\eta\xi}{(n+1)d_{SG}} \right], \quad (1)$$

where $d_{SG} = z_{\text{solvent-image}} - z_{\text{graphite-images}}$, $\eta = (\epsilon_v - \epsilon_G)/(\epsilon_v + \epsilon_G)$, and $\xi = (\epsilon_v - \epsilon_S)/(\epsilon_v + \epsilon_S)$. ϵ_v , ϵ_S and ϵ_G are the dielectric

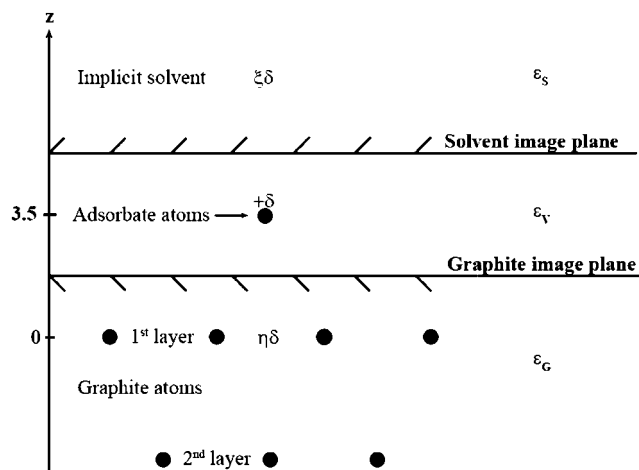


Figure 1. The implicit solvent model is represented as a dielectric medium with a dielectric constant of ϵ_S . ϵ_V and ϵ_G are the dielectric constants of the vacuum and graphite, respectively. The $+\delta$ charge is reflected through both the solvent and graphite image planes. The graphite and solvent image charges, $\eta\delta$ and $\xi\delta$, respectively, are in turn reflected again through the solvent and graphite image planes, respectively, and so on, leading to the infinite series in eq 1.

constants of the adsorbate, solvent and graphite layers, respectively. The dielectric constant of the adsorbate layer is that of the vacuum since the electrostatic interactions are calculated explicitly. In addition a repulsive potential of the form $u(z) = \epsilon(-5^6 + z^6)$; $z > 5$ was added to the MD simulations in the implicit solvent model to prevent divergences in the interactions of the adsorbate atoms and their image charges across the solvent image plane. We employ $\epsilon_G = 15$ and $\epsilon_S = 6$ (dielectric constant of undecanol) for the simulations using the implicit solvent model, and $\epsilon_G = 15$ and $\epsilon_S = 1$ (no dielectric above the adsorbate) for all the other simulations. The series in eq 1 was truncated at $n = 2$.

The explicit solvent model is represented by a single solvent layer on top of the adsorbate layer at full second layer coverage. Three different solvents are examined: an uncharged undecanol-like solvent, undecanol, and BrC_{20} . We have chosen undecanol, $\text{C}_{11}\text{H}_{24}\text{O}$, from among the experimentally studied solvents due to the relative simplicity of its modeling. In addition, a single layer of undecanol can provide, in general, a more uniform and less specific coverage of the adsorbate layer relative to the experimentally studied aromatic solvents. The single solvent layer is, nevertheless, exposed to vacuum. Additional solvent layers would have provided, in principle, additional ordering and confinement to the lowermost solvent layer. We note also that the dielectric constant of undecanol is 5.98. Although the polarizability varies considerably along the length of a single solvent chain, the standard OPLS-AA force field does not account for polarizability effects. The uncharged solvent is modeled after undecanol with the electrostatic charges switched off. The uncharged solvent layer had to be stabilized by enlarging the ϵ -parameters of the LJ potential for the hydrogen and oxygen atoms of the hydroxyl group. Otherwise, individual molecules from the uncharged solvent layer were observed to move independently and slide off the nonperiodic layer of adsorbate molecules toward the graphite surface.

Results

The Potential Energy Surface of BrC_{20} at the Graphite–Vacuum Interface. The principal driving force governing the ordering of alkane chains on surfaces is the fulfillment of close packing.

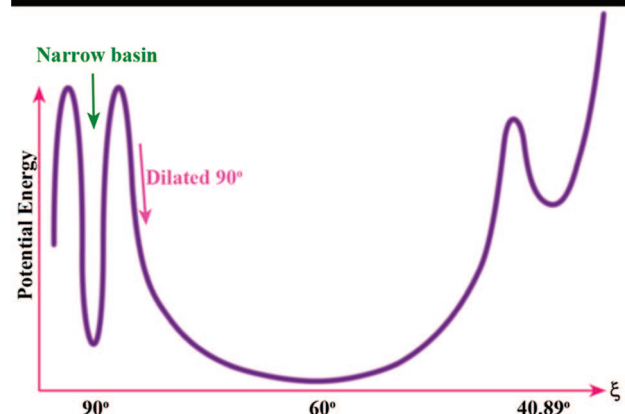
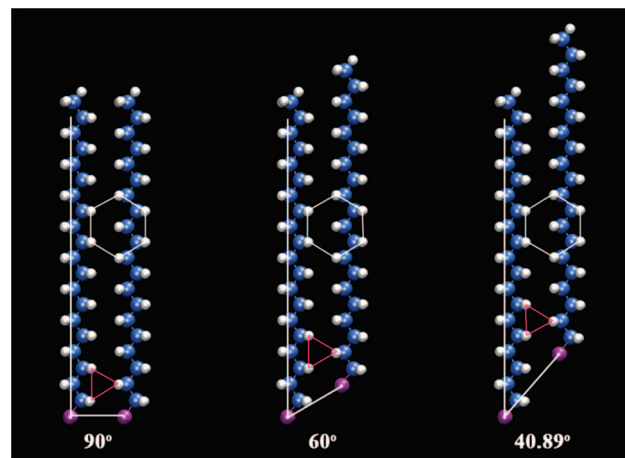


Figure 2. The series of lamella–backbone angles which satisfy the condition of close packing starts with 90° , 60° and 40.89° . The carbons, hydrogens, and bromines are colored blue, white, and purple, respectively. The hydrogen atoms form equilateral triangles (red) or equivalently hexagons (white). The potential energy is drawn schematically as a function of a generalized path coordinate, ξ , between the 90° , 60° and 40.89° lamella–backbone angles. Starting 90° configurations slightly off the minimum configuration (pink arrow) transform under vacuum to the 60° form. The barrier heights have not been estimated quantitatively.

Figure 2 displays three LB angles, 90° , 60° and 40.89° for which this condition is fulfilled. The series (90° , 60° , 40.89° , 30° , ...) is obtained by successively sliding neighboring chains (along the backbone axis) by one methylene group relative to each other.²¹ The hydrogen atoms thereby attain (white hexagons in Figure 2) a nearly perfect hexagonal arrangement. The hexagonal signature is generally observed in STM images of alkane derivatives on graphite since the electron density is dominated by the protruding hydrogen atoms.⁴⁶ The above series of LB angles was calculated by mapping the hydrogen atoms onto the graphite lattice, assuming perfect registry. The condition for close packing is, however, independent of the corrugation of the graphite lattice. In practice, slightly different LB angles will be measured according to the unit cell parameters of the adsorbate layer. The potential energy as a function of the LB angle is drawn schematically in Figure 2. The minima correspond to the minimum configurations at the LB angles for which the condition of close packing is satisfied. ξ is an arbitrary collective coordinate between the minimized configurations. The potential energy generally increases with decreasing LB angle. The features of the potential energy surface (PES) for BrC_{20} , i.e. the height and shape of the minima in Figure 2, are examined below.

We begin by characterizing the PES of the experimentally observed 60° and 90° LB morphologies, corresponding to those

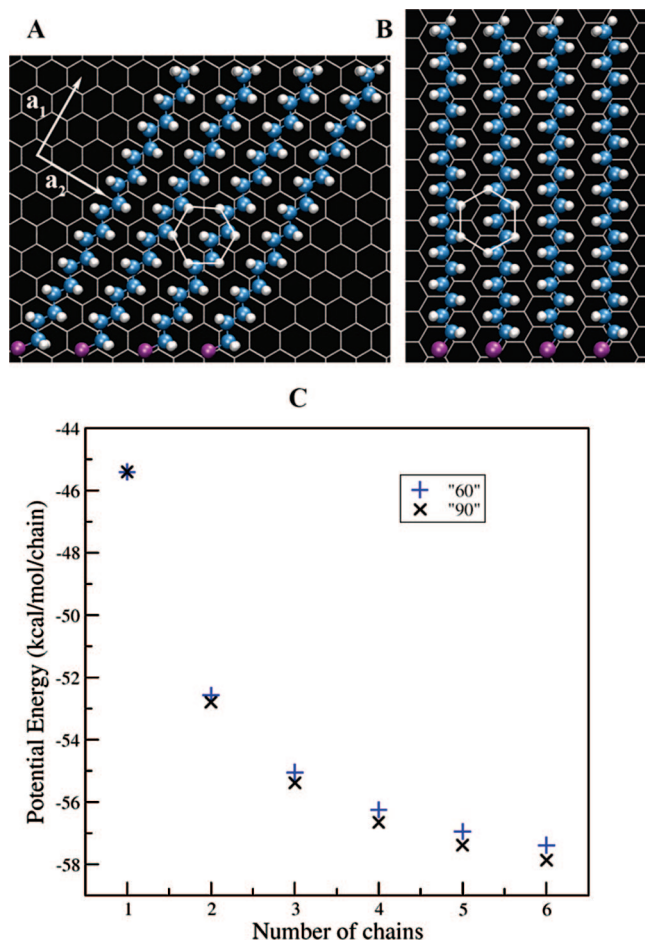


Figure 3. Configurations corresponding to the minimum of the PES ($N = 4$) under vacuum ($\epsilon_G = 15$) are displayed in A and B for the 60° and 90° forms, respectively. The BrC₂₀ chains are aligned along the a_1 vector of the graphite lattice and the interchain distances for both morphologies are measured along the a_2 vector. The alignment relative to the graphite lattice is very similar for both morphologies. The hydrogen atoms achieve a hexagonal arrangement for both configurations (white hexagons). The minima of the PES as a function of the number of chains, N , for the single lamella configuration are displayed in part C for the 60° (blue) and 90° (black) forms.

observed under UHV (80K and 245K) and solvent (298K) conditions, respectively (companion paper Part I).²⁴ The PES analysis was performed by minimizing starting 60° and 90° configurations under vacuum without periodic boundary conditions. Unfortunately, the analysis of the PES cannot be carried out under solvent conditions since it requires an averaging over all solvent configurations. The minimizations were carried out with the chains aligned (Figures 3A and 3B) along the principal, a_1 , vector of the graphite lattice (along the a_2 vector the minima of the potential energy are higher by approximately 1.5 kcal/mol/chain). They were interspersed with short simulated annealing runs (more so with increasing system size), and the lowest common minimum from different initial conditions was taken to be the minimum (in the neighborhood of a given LB angle).

We first consider single-lamella (SL) formations (Figure 3). The minima for the 60° and 90° SL configurations are plotted in Figure 3C against the number of chains, N . The 90° configurations are slightly more favorable (more so with increasing N). The image charge and LJ contributions to the potential energy of the 90° configuration are lower relative to the 60° configuration. The electrostatic contribution, on the other hand, is higher for 90° (e.g., Table 1, $N = 4$); the overall positive

electrostatic contribution is due to the geometrically constrained distribution of partial charges along the chain backbone. The interchain distance (measured perpendicular to the chain backbone) of the 60° configuration varies between 4.3 and 4.4 Å, at the tail and head regions, respectively, whereas that of the 90° form is approximately uniform at 4.35 Å. The hydrogen atoms, for both morphologies, are positioned approximately above the centers of the graphite hexagons, thereby adopting an approximate hexagonal geometry. This packing configuration was predicted nearly forty years ago by Groszek,⁴⁷ based on adsorption isotherm measurements of long n -alkane chains from solution. The hydrogen atoms of the peripheral chains are slightly shifted relative to the centers of the graphite carbons, reflecting the larger vdW radius of the alkane carbons relative to the graphite carbons. It is not clear, therefore, whether a larger array of BrC₂₀ molecules can pack commensurably with the graphite lattice, and even less so at finite temperatures. We return to this issue below.

We now consider head-to-head double-lamella (DL) formations (Figure 4). The DL configuration ($N = 8$) is favorable relative to the SL configuration ($N = 4$) for both the 90° and 60° morphologies, by approximately 0.2 kcal/mol/chain and 1 kcal/mol/chain, respectively. The potential energy of the minimized DL 60° form, -57.28 kcal/mol/chain, is slightly lower than that of the DL 90° at -56.82 kcal/mol/chain. The next LB angle for which the chains observe close-packing is 40.89° (Figure 2). The minimum of the potential energy at 40.89°, -55.92 kcal/mol/chain, is higher by more than 1 kcal/mol/chain relative to both the 90° and 60° forms. The energy minimized configurations of the DL 90° and 60° geometries are displayed in Figures 4A and 4B, respectively. The interchain distance at the head region increases to 4.46 Å for both the 60° and 90° forms. Lamellae are separated by approximately 2.8 Å (the width of the trough—along the y -axis), and the reversed orientation of the bromines (on opposite lamella) is energetically favorable. The chains (including the terminal C–Br vectors) lie parallel to the surface in the extended all-trans configuration.

The breakdown of the potential energy into its various contributions for the SL and DL configurations of the 90° and 60° LB angles, for representative values of the dielectric constants of the graphite and the implicit solvent, is compiled in Table 1. The SL-to-DL stabilization for the 60° form arises mostly due to favorable LJ contribution (Table 1, second versus eighth row). The electrostatic energy is nearly independent of the transition from SL to DL (slightly more so for the 60° than the 90° configuration). Another interesting observation is that the potential energy of the 90° geometry decreases more rapidly with increasing dielectric constant. Between the two limiting cases, given by $\epsilon_G = 1$, $\epsilon_S = 1$, and $\epsilon_G = \infty$, $\epsilon_S = \infty$, (Table 1, fifth and sixth versus 13th and 14th rows) respectively, the potential energy is offset in favor of the DL 90° relative to the DL 60° by approximately 1.2 kcal/mol/chain. The offset arises almost exclusively from the image charge contribution (which is separate from the electrostatic contribution). The other contributions to the potential energy are largely invariant with respect to the dielectric fields. The favorable image charge interactions of the 90° geometry for both the SL and DL is mainly due to the orientation of the dipole moments of the head groups. While variations of 1 kcal/mol/chain or less may seem rather negligible they can account for a substantial percentage of the total potential energy when the Steele contribution is factored out.

The convergence to the minimum is achieved exceptionally slowly for the DL 90° configurations. This suggests that the

TABLE 1: Breakdown of the Total Potential Energy into Various Contributions^a

	structure	total	stretch	bend	torsion	electrostatic	LJ	Steele	image charge
1	90° SL $N = 4$ $\epsilon_G = 15$ $\epsilon_S = 1$	-56.6468	0.1089	1.6946	0.2122	6.1888	-12.1261	-51.4518	-1.2733
2	60° SL $N = 4$ $\epsilon_G = 15$ $\epsilon_S = 1$	-56.2512	0.1089	1.6957	0.2173	5.5723	-11.5658	-51.4439	-0.8358
3	90° SL $N = 4$ $\epsilon_G = \infty$ $\epsilon_S = 1$	-56.8296	0.1085	1.6943	0.2131	6.1943	-12.1259	-51.4435	-1.4704
4	60° SL $N = 4$ $\epsilon_G = \infty$ $\epsilon_S = 1$	-56.3711	0.1086	1.6957	0.2184	5.5736	-11.5639	-51.4401	-0.9634
5	90° DL $N = 8$ $\epsilon_G = 1$ $\epsilon_S = 1$	-55.7306	0.0940	1.7800	0.2077	6.2066	-12.6613	-51.3575	0.0000
6	60° DL $N = 8$ $\epsilon_G = 1$ $\epsilon_S = 1$	-56.8915	0.1109	1.7020	0.2103	5.3079	-12.7896	-51.4331	0.0000
7	90° DL $N = 8$ $\epsilon_G = 15$ $\epsilon_S = 1$	-56.8164	0.1181	1.7041	0.2187	6.3956	-12.3908	-51.4441	-1.4180
8	60° DL $N = 8$ $\epsilon_G = 15$ $\epsilon_S = 1$	-57.2804	0.1011	1.6915	0.2231	5.5832	-12.6055	-51.4423	-0.8317
9	90° DL $N = 8$ $\epsilon_G = \infty$ $\epsilon_S = 1$	-57.0643	0.0890	1.7141	0.2288	6.3105	-12.6645	-51.2862	-1.4565
10	60° DL $N = 8$ $\epsilon_G = \infty$ $\epsilon_S = 1$	-57.4001	0.1008	1.6913	0.2253	5.5867	-12.6033	-51.4385	-0.9622
11	90° DL $N = 8$ $\epsilon_G = 15$ $\epsilon_S = 6$	-57.7172	0.1261	1.7039	0.2182	6.4368	-12.4236	-51.4623	-2.3162
12	60° DL $N = 8$ $\epsilon_G = 15$ $\epsilon_S = 6$	-57.8758	0.1050	1.6879	0.2222	5.5945	-12.6154	-51.4525	-1.4175
13	90° DL $N = 8$ $\epsilon_G = \infty$ $\epsilon_S = \infty$	-58.2620	0.1304	1.7070	0.2243	6.4624	-12.4336	-51.4568	-2.8957
14	60° DL $N = 8$ $\epsilon_G = \infty$ $\epsilon_S = \infty$	-58.2280	0.1068	1.6873	0.2277	5.6044	-12.6142	-51.4523	-1.7877

^a The energy units are in kcal/mol/chain. SL = single lamella. DL = double lamella. N is the number of chains in the lamella. ϵ_G and ϵ_S are the dielectric constants of graphite and solvent, respectively.

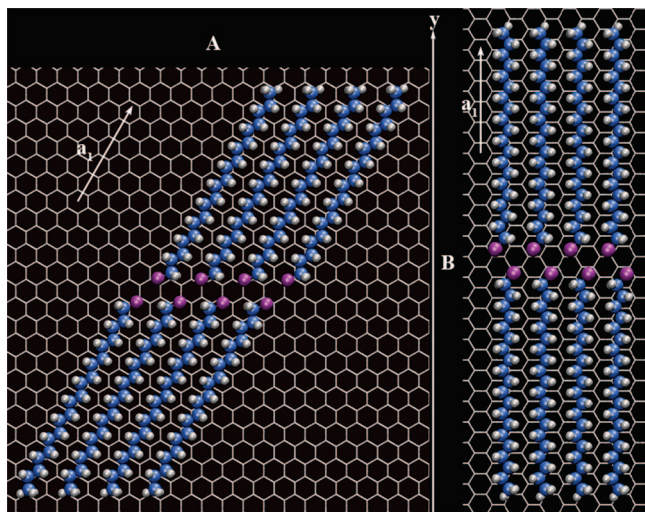


Figure 4. Minimum configurations of the PES ($N = 8$, double lamella) under vacuum ($\epsilon_G = 15$) are displayed in A and B for the 60° and 90° forms, respectively. The distance between the bromines in opposite lamellae, along the y -axis, is ~ 2.75 Å and ~ 2.9 Å for the 60° and 90° forms, respectively.

basin of the PES about the DL 90° configuration is narrow and possibly surrounded by a rough and insurmountable landscape (see Figure 2 for a schematic illustration). This feature of the PES suggests that the 90° form is less likely to be accessible, relative to the 60° geometry, under UHV conditions since the vacuum deposition process is expected to be more rapid. In summary the PES of BrC₂₀ on graphite reveals two approximately degenerate minima characterized by dissimilar landscapes about the 60° and 90° morphologies. The packing densities of the 60° and 90° formations are very similar.

The Free Energy Surface of BrC₂₀ at the Graphite–Vacuum Interface. Simulations of the 60° and 90° forms for a total of 72 chains were performed under vacuum without periodic boundary conditions at $T = 80$ K and $T = 298$ K. The 60° morphology is stable at both temperatures. At $T = 80$ K the simulated structures are approximately close-packed (Figure 5A), whereas at $T = 298$ K they exhibit slight fluctuations about the ideal configuration (Figure 5B), and the average interchain distance increases by approximately 0.2 Å. By close-packing we refer here to the minimized configuration (Figure 4). The simulated interchain distances at 80 K compare well with experimentally measured distances for BrC₆ under vacuum conditions.¹⁷ A reliable estimate of the average interchain

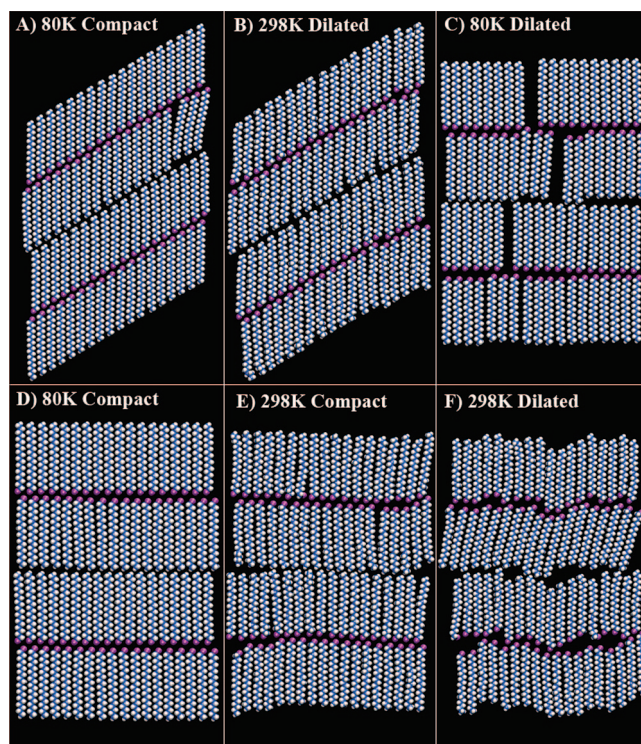


Figure 5. Simulation snapshots of BrC₂₀ under vacuum ($\epsilon_G = 15$) are displayed for the following conditions: (A) $T = 80$ K, 85 ps, starting configuration is 60° compact; (B) $T = 298$ K, 85 ps, starting configuration is 60° dilated; (C) $T = 80$ K, 58 ps, starting configuration is 90° dilated; (D) $T = 80$ K, 58 ps, starting configuration is 90° compact; (E) $T = 298$ K, 110 ps, starting configuration is 90° compact; (F) $T = 298$ K, 129 ps, starting configuration is 90° dilated. All the simulations are performed with the chains in the initial configurations aligned along the a_1 axis (graphite lattice not displayed). The alignment is generally maintained (but for a small tilt of the second row in part F).

distance for BrC₂₀ under UHV conditions could not be extracted due to a degree of disorder in the self-assembled monolayer. The 90° morphology, on the other hand, has been observed to be unstable for starting configurations slightly off the minimum. Such configurations were obtained, for example, by dilating the starting interchain distance to 5 Å. In addition, at $T = 298$ K, the 90° formation was observed to destabilize even for a compact starting interchain distance of 4.5 Å when the alignment of the opposing bromines did not closely follow the minimized DL configuration (Figure 4B). In what follows we shall use the

terms dilated and compact to describe starting configurations with interchain distances of 5 and 4.5 Å, respectively. At $T = 80$ K, for dilated starting configurations, the 90° form exhibits local domains of close-packed ordering (Figure 5C). For compact starting configurations, the ordering is maintained (Figure 5D). At $T = 298$ K, compact 90° starting configurations maintain ordering for at least 100 ps (Figure 5E). In contrast, the dilated configurations disorder appreciably within a few ps and undergo a phase transition to a stable 60° geometry. The snapshot in Figure 5F corresponds to 129 ps and displays the initial stages of the ordering transition.

The 60° and the dilated 90° forms remain stable and unstable, respectively, when the corrugation of the graphite lattice is switched off ($T = 298$ K). The symmetry of the graphite lattice is compatible with the 60° and 90° LB angles; the corrugation, therefore, is expected to further stabilize the 60° and 90° morphologies and consequently raise the 90°-to-60° transition barrier. In addition, the corrugation could manifest itself, in principle, through modification of the inter- and intrachain distances from their bulk values to possibly accomplish registry of the adsorbate layer with the graphite lattice. The dilated 90°-to-60° transition time scale ($T = 298$ K) is ~ 1 ns and 100–200 ps for the corrugated and noncorrugated graphite lattice, respectively. The larger transition barrier associated with the corrugated surface is consistent with the large Steele contribution to the potential energy (Table 1) and the preservation of epitaxy at temperatures considerably higher than the melting temperature of the bulk crystal.⁴⁸ The transition timescales have been estimated from a few simulations of smaller clusters of BrC₂₀. They do not reflect the escape from the bottom of the basin, corresponding to the minimized configuration of the 90° form, since the starting 90° configurations are dilated. Otherwise it would have been possible to estimate the magnitude of the transition barrier between the minima of the 90° and 60° geometries from transition state theory.

The backbone skeleton remains parallel to the graphite surface at all times within the 60° phase and the close-packed stable 90° form and throughout the dilated 90°-to-60° transition. In particular, the terminal vector connecting the bromine with the carbon exhibits very little fluctuation. The approximately fixed distance between the Br atoms and the graphite surface is due to the value of its LJ ϵ parameter which is larger by a factor of approximately 7 and 16 relative to that of carbon and hydrogen, respectively. The bromine atom serves essentially as an extension of the chain backbone. The parallel orientation of the terminal vector confines the head-to-head interactions to a two-dimensional plane thereby accentuating variations in the PES as a function of the LB angle. The large polarizability and dipole moment associated with the Br atoms suggest a highly specific interdigitated alignment of the head-to-head groups in analogy with teeth-like processes such as those in a timing belt or a zipper. A rare and energetically unfavorable flip of the orientation of one of the bromines is observed (top row of Figure 5E and second row from the bottom of Figure 5F). The dilated 90°-to-60° transition pathway varies depending on whether the chains in the initial 90° configuration are aligned along the a_2 or a_1 graphite axes. For the former setup, the chains reorient by 30° to the a_1 axis whereas for the latter they more or less maintain their orientation while sliding with respect to each other (Figure 5F). The small tilt of the second row in Figure 5F is transient and the chains in the final 60° form are expected (from longer simulations on smaller systems) to maintain alignment along the original a_1 vector. The dilated 90°-to-60° pathway, observed for a noncorrugated graphite lattice at $T = 298$ K,

proceeds with local 60° geometries forming and stabilizing each other in a collective manner.

The origin of the narrow basin of the PES about the 90° geometry may be understood by inspecting the optimized DL configurations (Figure 4). Imagining a uniformly dilated 90° DL configuration, the intermolecular and head-to-head spacings must be compressed more or less simultaneously in order to achieve the close-packed configuration; similarly a zipper can not be fastened by brute force compression. At the 60° geometry, on the other hand, the bromine atoms are nestled in between the hydrogen atoms of methyl groups of neighboring chains. Therefore, opposing Br atoms in the 60° formation do not incur penalties due to the interpenetration of their LJ spheres at finite temperatures. In addition, the alignment of the dipole moments of the Br head groups at the 60° formation is favorable relative to that of 90°.

Marchenko and Cousty have characterized the stability of the 60° and 90° forms for *n*-alkanes on Au(111) by calculating the sliding forces along the Au(111) principal vectors.²² For chain lengths incommensurate with the superposition of the spacing of Au(111) and the alkane backbone, they find the barrier for the formation of the 90° geometry to be large, accounting for increased coverage of the surface by domains of the 60° form. The analogy, however, between graphite and Au(111), and 1-haloalkane and *n*-alkane is incomplete. Unlike the case for Au(111), the lattice spacing of graphite (2.46 Å) matches the corresponding spacing along the alkane backbone (2.51 Å) very well. Different substrates may even induce different self-assembly morphologies for the same molecule.^{2,49} Dotriacontane (C₃₂H₆₆), for example, displays 60° and 90° morphologies on transition-metal dichalcogenides (MoS₂, MoSe₂), and graphite, respectively.^{2,49}

In summary, the basin of the PES about the minimum of the DL 90° form is very narrow. This narrow basin manifests itself in a free energy landscape that is likely to sample the 60° morphology at finite temperatures in agreement with the STM findings under UHV conditions.^{17,24}

Implicit Solvent Model. Simulations of BrC₂₀ using the implicit solvent model were carried out at $T = 298$ K, for starting dilated 60° and 90° configurations. The implicit solvent model further orders (not shown) the 60° form relative to the corresponding vacuum simulation, and the average interchain distance is compressed slightly to ~ 4.6 Å from the starting interchain distance of 5 Å. The dilated 90° form, while not exhibiting a transition to 60° anymore, displays local disorder about the bromines. The observation that the dilated 90°-to-60° transition does not take place or is slowed down appreciably under the implicit solvent model is drawn from simulation studies of smaller clusters of BrC₂₀. Although the dilated 90°-to-60° transition is inhibited, the dilated 90° geometry does not attain close-packing with an implicit solvent field, whereas the corresponding STM images under solvent display a highly ordered 90° phase.²⁴ In addition, the dilated 90° form can be stabilized to its close-packed configuration ($T = 298$ K) using an uncharged explicit solvent model (see following section), suggesting that the electrostatic components of the solvent-adsorbate interactions may not be important. The flat image plane at the interface between the solvent and adsorbate layers is a rudimentary model of the solvent reaction field, mirroring the adsorbate charges only along the z -axis (Figure 1). In principle, it may be possible to further order the 90° configuration by improving upon the implicit solvent model, for

example, by replacing the flat image plane with an image manifold that adapts locally to the shape of the BrC₂₀ molecules.⁵⁰

In summary, the implicit solvent model is not sufficient to order the dilated 90° form to its close-packed phase at $T = 298$ K, however, it does prevent the dilated 90°-to-60° transition from occurring (or slows it down appreciably), possibly by lowering the effective temperature experienced by the adsorbate. The implicit solvent model is successful in that it lowers the potential energy of the 90° phase relative to that of the 60° form (Table 1).

Explicit Solvent Model. Simulations of the explicit solvent model are performed at $T = 298$ K without periodic boundary conditions using a single solvent layer on top of the adsorbate layer (for a total of 56 BrC₂₀ molecules). Simulation snapshots for the uncharged and charged undecanol solvent are displayed in parts A and B of Figure 6, respectively, initiated from dilated 90° configurations for both the solvent and adsorbate layers. Figure 6C corresponds to BrC₂₀ under undecanol started from a dilated 60° configuration. For the 60° form, a repulsive potential was imposed above the undecanol layer, otherwise the chains would jut into the vacuum. Undecanol clearly has the effect of stabilizing the 90° morphology (Figure 6B) in agreement with experiment, and the average interchain distance of BrC₂₀ at $T = 298$ K is approximately at the close-packed value of 4.5 Å. The experimentally measured interchain distance under solvent is approximately 4.4 Å.²⁴ The discrepancy between theory and experiment, although small in magnitude, may reflect the preassigned values of the vdW radii in our classical simulations, or the inclusion of only a single layer of solvent. Although 4.5 Å is larger than the value required for commensurability with the graphite lattice, 4.26 Å, the compression by 0.15 Å from the average interchain distance under vacuum (at the same temperature $T = 298$ K) is likely driven to a large extent by the condition for registry. Enlarging the head-to-head region (Figure 6, right column) suggests that the solvent and the adsorbate layers can arrange themselves in various ways with respect to each other to achieve commensurate ordering and mutual stabilization. These arrangements may be considered as degenerate minima on the PES of the composite solvent and adsorbate system at 90°.

Undecanol, however, does not induce a 60°-to-90° transition (Figure 6C). It is not clear, therefore, why the experimentally observed morphology of BrC₂₀ for a wide range of solvents is 90° and not 60°. One possible explanation is that the 90° morphology provides a superior template for solvent capping: the higher symmetry of the 90° form allows solvents in general to accommodate periodically and mediate the head-to-head interactions. In other words, in addition to asking what the solvent can do for the solute, we should also be asking what the solute can do for the solvent. Several observations lend support to this interpretation. First, when the solvent is taken to be BrC₂₀, the composite double-layered BrC₂₀ system is unstable at 90° and may even undergo a dilated 90°-to-60° transition at longer simulation times, since in this case the symmetry preferred by the dilated solvent is obviously the 60° form. Second, the symmetry principle does not hold for the structureless implicit solvent. Another possibility is that the deposition process of the adsorbate from the solvent is more likely to start with an approximately 90° LB ordering of the chains. The solvent induced stabilization, in contrast to the UHV deposition process, would trap the 90° form and inhibit any further transition to the 60° morphology. The solvent deposition process is also much slower relative to the deposition under

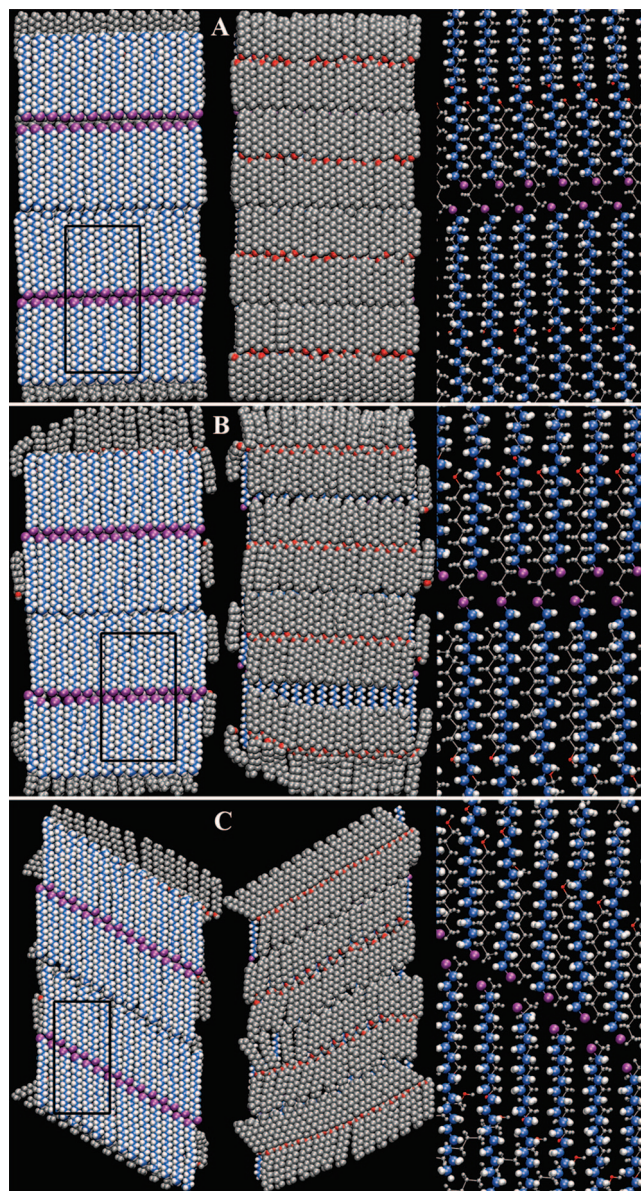


Figure 6. Representative snapshots of the explicit solvent studies, with 56 adsorbate (BrC₂₀) and 112 solvent (undecanol) molecules, are displayed in A, B and C for the uncharged undecanol with a 90° starting configuration (122 ps), charged undecanol with 90° starting configuration (96 ps), and charged undecanol with 60° starting configuration (91 ps), respectively ($T = 298$ K). Left, middle and right columns correspond to bottom view, top view, and an enlargement of the black squared regions, respectively. The carbons and hydrogens of the solvent are in silver and the oxygens are red.

UHV allowing the self-assembly process more time to explore optimal morphologies on the PES. The relatively large number of head-to-tail 'defects' observed in the STM image of the 60° form suggests kinetic traps during the faster self-assembly process under UHV conditions (see companion paper Part I)²⁴ Finally, the implicit solvent model offsets the potential energy in favor of the 90° morphology, thereby providing also a thermodynamic argument for the observation of the 90° form under solvent.

The extraction of conclusions and principles from a few simulation studies of putative configurations for the composite solvent/adsorbate system must be viewed with some care. For example, the positioning of the hydroxyl groups of the undecanol relative to the headgroups of the BrC₂₀ in Figure 6 is arbitrary, since the lengths of the undecanol and BrC₂₀ are not rational

multiples of each other. In addition, the parallel alignment of the undecanol relative to the BrC₂₀ is also rather arbitrary. In a study of a solution of *n*-C₃₆H₇₄ in decane on graphite, a bilayer was observed with the second layer rotated by 60° with respect to the first layer.⁵¹ It is also possible that the adsorbate layer explores alternative configurations in the presence of solvent. For example, some of the chains may not be lying flat on the graphite surface. To test the latter possibility, we ran starting DL 90° configurations of BrC₂₀ under undecanol (*T* = 298 K) with various out-of-plane angles, ±35°, ±45°, and ±50° (rotation about the backbone axis). For a ±35° configuration the BrC₂₀ rotated back to lie flat (zigzag backbone lies parallel to the graphite surface), whereas for the ±50° angle, the BrC₂₀ rotated so as to lie perpendicular to the graphite surface with the bromines facing either up or down depending on the sign of the initial angular distribution. At ±45° both parallel and perpendicular domains were observed. The perpendicular formation maintains more or less the 90° LB alignment yet exhibits strong disorder about the headgroups, and the average interchain distance decreases to 3.9 Å. The disorder about the headgroup for the perpendicular geometry is also dependent on how the terminal C–Br vectors of neighboring chains are oriented with respect to the graphite surface (in opposite directions or together, either away or toward the surface).

An alternating parallel and perpendicular formation has been invoked in a neutron diffraction study to possibly explain the compression of *n*-C₃₂D₆₆ that takes place upon transition from vapor to solvent deposition.⁵² In addition, Krishnan et al. have simulated the transition of *n*-hexanes to registry with the graphite substrate upon coverage.^{18,19} A few perpendicular orientations of the *n*-hexanes were observed at single layer coverage, whereas all of the chains oriented parallel to the graphite surface at trilayer coverage.^{18,19} We do not observe any spontaneous parallel-to-perpendicular reorientation in our simulations under both vacuum and solvent conditions, due to the presence of the heavy and polarizable Br atom and the length of our chains. Our simulations also display a registry transition upon coverage with solvent. The average interchain distance of the 60° arrangement under vacuum is larger by ~4% relative to that of the 90° form under solvent (at *T* = 298 K). A similar compression of the average interchain distance by ~7% was observed for *n*-hexane upon coverage.^{18,19} A heuristic study by Khandkar and Balasubramanian of a monatomic LJ fluid (argon) on a corrugated surface depicted a lateral isotropic compression of ~2% upon single to bilayer coverage.⁵³ The strong driving force associated with registry is also illustrated by the commensurability of the interchain distance of *n*-alkanes on Au(111). The distance between second neighbor (110) rows of Au atoms is larger than the corresponding interchain distance of bulk alkanes (the interchain distance of *n*-alkanes on graphite is, on the other hand, compressed from the bulk phase).²² In contrast, Zhang et al. report an interchain value commensurate with the spacing of the *n*-alkanes in their bulk phase following surface reconstruction of the Au(111).²³ Studies of alkane and alkanol monolayers on graphite and MoS₂ display nearly identical angles and distances despite the significantly different lattice spacing of MoS₂ and graphite.⁵⁴ The influence of the substrate on the self-assembly morphology of functionalized hydrocarbons on MoS₂ and graphite has also been studied systematically.²

Conclusions

The framework for understanding the phase ordering of BrC₂₀ on graphite is the fulfillment of a close packing arrangement at the 60° and 90° LB angles. This work has centered on

characterizing the stabilities of the 60° and 90° forms under UHV and solvent conditions. The potential energy of the DL 90° morphology is slightly higher than that of the DL 60° form under vacuum. In addition, the basin of the PES about the minimum of the 90° arrangement is likely very narrow suggesting that the 90° form is not likely to be sampled through a fast deposition process in agreement with the UHV experimental studies. An explicit solvent model stabilizes the 90° form in the sense that starting off-minimum configurations, in contrast to the situation under vacuum, exhibit compression to the close-packed state. The explicit solvent model therefore effectively widens the basin of the PES about the 90° form. The 60° configuration is stable under both vacuum and solvent conditions. The observation of the 90° form under ambient solvent conditions may be due to either the self-assembly pathway or the superior template offered by this symmetry.

The polarizable bromine atoms tend to cluster in a head-to-head pattern,^{17,24} yet they are also responsible for the instability of the 90° configuration. The failure of the implicit solvent model to stabilize the 90° form by mitigating the dipole interactions of the opposing head-to-head groups is perhaps surprising. This failure may be due to the simplicity of our implicit solvent model, yet the 90° form can also be stabilized by a vdW (chargeless) solvent. The failure of the implicit solvent model suggests that the narrowness of the PES about the 90° geometry may be due to unfavorable dispersion interactions arising from the interpenetrations of bromine atoms from across opposite lamellae. The solvent dispersion field appears, therefore, to be both necessary and sufficient for the stabilization and uniaxial compression^{18,19,53} of the 90° configuration. Nevertheless, the solvent dielectric field offsets the total potential energy in the right direction, in favor of the 90° form.

Acknowledgment. We would like to thank Harry A. Stern and David Rinaldo for stimulating discussions. This work was supported by the National Science Foundation under Grants CHE-06-13401 (to B.J.B.) and CHE-07-01483 (to G.W.F.), by the NSEC Program under Grant CHE-06-41523, by the New York State Office of Science, Technology, and Academic Research (NYSTAR), by the U.S. Department of Energy at Brookhaven National Laboratory (DE-AC02-98CH10886 to M.S.H) and by the Clare Boothe Luce Program of the Henry Luce Foundation, Inc. (to G.M.F.).

References and Notes

- (1) De Feyter, S.; De Schryver, F. C. Two-dimensional supramolecular self-assembly probed by scanning tunneling microscopy. *Chem. Soc. Rev.* **2003**, *32* (6), 393–393.
- (2) Giancarlo, L. C.; Fang, H. B.; Rubin, S. M.; Bront, A. A.; Flynn, G. W. Influence of the substrate on order and image contrast for physisorbed, self-assembled molecular monolayers: STM studies of functionalized hydrocarbons on graphite and MoS₂. *J. Phys. Chem. B* **1998**, *102* (50), 10255–10263.
- (3) Binning, G.; Rohrer, H.; Gerber, C.; Weibel, E. Surface Studies by Scanning Tunneling Microscopy. *Phys. Rev. Lett.* **1982**, *49* (1), 57–61.
- (4) Giancarlo, L.; Cyr, D.; Muyskens, K.; Flynn, G. W. Scanning tunneling microscopy of molecular adsorbates at the liquid-solid interface: Functional group variations in image contrast. *Langmuir* **1998**, *14* (6), 1465–1471.
- (5) Giancarlo, L. C.; Flynn, G. W. Raising flags: Applications of chemical marker groups to study self-assembly, chirality, and orientation of interfacial films by scanning tunneling microscopy. *Acc. Chem. Res.* **2000**, *33* (7), 491–501.
- (6) Wintgens, D.; Yablon, D. G.; Flynn, G. W. Packing of HO(CH₂)₁₄COOH and HO(CH₂)₁₅COOH on graphite at the liquid-solid interface observed by scanning tunneling microscopy: Methylene unit direction of self-assembly structures. *J. Phys. Chem. B* **2003**, *107* (1), 173–179.
- (7) Kampschulte, L.; Lackinger, M.; Maier, A. K.; Kishore, R. S. K.; Griessl, S.; Schmittel, M.; Heckl, W. M. Solvent induced polymorphism in

supramolecular 1,3,5-benzenetribenzoic acid monolayers. *J. Phys. Chem. B* **2006**, *110* (22), 10829–10836.

(8) Lackinger, M.; Griessl, S.; Heckl, W. A.; Hietschold, M.; Flynn, G. W. Self-assembly of trimesic acid at the liquid-solid interface—a study of solvent-induced polymorphism. *Langmuir* **2005**, *21* (11), 4984–4988.

(9) Yablon, D. G.; Giancarlo, L. C.; Flynn, G. W. Manipulating self-assembly with achiral molecules: An STM study of chiral segregation by achiral adsorbates. *J. Phys. Chem. B* **2000**, *104* (32), 7627–7635.

(10) Crystal, J.; Zhang, L. Y.; Friesner, R. A.; Flynn, G. W. Computational Modeling for scanning tunneling microscopy of physisorbed molecules via ab initio quantum chemistry. *J. Phys. Chem. A* **2002**, *106* (9), 1802–1814.

(11) Claypool, C. L.; Faglioni, F.; Goddard, W. A.; Gray, H. B.; Lewis, N. S.; Marcus, R. A. Source of image contrast in STM images of functionalized alkanes on graphite: A systematic functional group approach. *J. Phys. Chem. B* **1997**, *101* (31), 5978–5995.

(12) Faglioni, F.; Claypool, C. L.; Lewis, N. S.; Goddard, W. A. Theoretical description of the STM images of alkanes and substituted alkanes adsorbed on graphite. *J. Phys. Chem. B* **1997**, *101* (31), 5996–6020.

(13) Cheng, A.; Klein, M. L. Melting Transition of Ethylene on Graphite. *Langmuir* **1992**, *8* (11), 2798–2803.

(14) Cincotti, S.; Burda, J.; Hentschke, R.; Rabe, J. P. Calculation of Monolayer Structures of Hydrocarbon Chains on Transition-Metal Dichalcogenides - Dotriacontane on MoS₂. *Phys. Rev. E: Stat., Nonlinear, Soft Matter Phys.* **1995**, *51* (3), 2090–2098.

(15) Xie, Z. X.; Xu, X.; Tang, J.; Mao, B. W. Molecular packing in self-assembled monolayers of normal alkane on Au(111) surfaces. *Chem. Phys. Lett.* **2000**, *323* (3–4), 209–216.

(16) Florio, G. M.; Werblowsky, T. L.; Müller, T.; Berne, B. J.; Flynn, G. W. Self-assembly of small polycyclic aromatic hydrocarbons on graphite: A combined scanning tunneling microscopy and theoretical approach. *J. Phys. Chem. B* **2005**, *109* (10), 4520–4532.

(17) Müller, T.; Werblowsky, T. L.; Florio, G. M.; Berne, B. J.; Flynn, G. W. *Proc. Nat. Acad. Sci. U.S.A.* **2005**, *102* (15), 5315–5322.

(18) Krishnan, M.; Balasubramanian, S.; Clarke, S. Structure of solid monolayers and multilayers of *n*-hexane on graphite. *Proc. Ind. Acad. Sci.—Chem. Sci.* **2003**, *115* (5–6), 663–677.

(19) Krishnan, M.; Balasubramanian, S.; Clarke, S. An atomistic simulation study of a solid monolayer and trilayer of *n*-hexane on graphite. *J. Chem. Phys.* **2003**, *118* (11), 5082–5086.

(20) Arnold, T.; Dong, C. C.; Thomas, R. K.; Castro, M. A.; Perdigon, A.; Clarke, S. M.; Inaba, A. The crystalline structures of the odd alkanes pentane, heptane, nonane, undecane, tridecane and pentadecane monolayers adsorbed on graphite at submonolayer coverages and from the liquid. *Phys. Chem. Chem. Phys.* **2002**, *4* (14), 3430–3435.

(21) Kitaigorodskii, A. I., *Molecular crystals and molecules*; Academic Press: New York, 1973.

(22) Marchenko, A.; Cousty, J. “Magic size” effect in the packing of *n*-alkanes on Au(111): evidence of lowered sliding force for molecules with specific length. *Wear* **2003**, *254* (10), 941–944.

(23) Zhang, H. M.; Xie, Z. X.; Mao, B. W.; Xu, X. Self-assembly of normal alkanes on the Au(111) surfaces. *Chem.—Eur. J.* **2004**, *10* (6), 1415–1422.

(24) Florio, G. M.; Ilan, B.; Müller, T.; Baker, T. A.; Rothman, A.; Werblowsky, T. L.; Flynn, G. W. Solvent Effects on the Self-Assembly of 1-Bromoeicosane on Graphite. Part I: Scanning Tunneling Microscopy. *J. Phys. Chem. C* **2009**, *113* (9), 3631–3640.

(25) Müller, T.; Flynn, G. W.; Mathauer, A. T.; Teplyakov, A. V. Temperature-programmed desorption studies of *n*-alkane derivatives on graphite: Desorption energetics and the influence of functional groups on adsorbate self-assembly. *Langmuir* **2003**, *19* (7), 2812–2821.

(26) Florio, G. M.; Werblowsky, T. L.; Ilan, B.; Müller, T.; Berne, B. J.; Flynn, G. W., Chain-length effects on the self-assembly of short 1-bromoalkane and *n*-alkane monolayers on graphite. *J. Phys. Chem. C* **2008**.

(27) Pasquarello, A.; Hybertsen, M. S.; Car, R. Theory of Si 2p core-level shifts at the Si(001)-SiO₂(2) interface. *Phys. Rev. B: Condens. Matter Mater. Phys.* **1996**, *53* (16), 10942.

(28) Yablon, D. G.; Wintgens, D.; Flynn, G. W. Odd/even effect in self-assembly of chiral molecules at the liquid-solid interface: An STM investigation of coadsorbate control of self-assembly. *J. Phys. Chem. B* **2002**, *106* (21), 5470–5475.

(29) Jorgensen, W. L. Optimized Intermolecular Potential Functions for Liquid Alcohols. *J. Phys. Chem.* **1986**, *90* (7), 1276–1284.

(30) Udier-Blagovic, M.; De Tirado, P. M.; Pearlman, S. A.; Jorgensen, W. L. Accuracy of free energies of hydration using CM1 and CM3 atomic charges. *J. Comput. Chem.* **2004**, *25* (11), 1322–1332.

(31) Hay, P. J.; Wadt, W. R. Abinitio Effective Core Potentials for Molecular Calculations - Potentials for K to Au Including the Outermost Core Orbitals. *J. Chem. Phys.* **1985**, *82* (1), 299–310.

(32) Becke, A. D. Density-Functional Thermochemistry 0.3. The Role of Exact Exchange. *J. Chem. Phys.* **1993**, *98* (7), 5648–5652.

(33) Lee, C. T.; Yang, W. T.; Parr, R. G. Development of the Colle-Salvetti Correlation-Energy Formula into a Functional of the Electron-Density. *Phys. Rev. B: Condens. Matter Mater. Phys.* **1988**, *37* (2), 785–789.

(34) Jaguar 6.5, Schrödinger, LLC, New York, NY, 2005.

(35) Jorgensen, W. L. In *Encyclopedia of Computational Chemistry*, Schleyer, P. v. R., Ed.; Wiley: New York, 1998; Vol. 5, pp 3281–3285.

(36) Dewar, M. J. S.; Zoebisch, E. G.; Healy, E. F.; Stewart, J. J. P. The Development and Use of Quantum-Mechanical Molecular-Models 0.76. Am1—a New General-Purpose Quantum-Mechanical Molecular-Model. *J. Am. Chem. Soc.* **1985**, *107* (13), 3902–3909.

(37) Stewart, J. J. P. Optimization of Parameters for Semiempirical Methods 0.1. Method. *J. Comput. Chem.* **1989**, *10* (2), 209–220.

(38) Steele, W. A. Physical Interaction of Gases with Crystalline Solids 0.1. Gas-Solid Energies and Properties of Isolated Adsorbed Atoms. *Surf. Sci.* **1973**, *36* (1), 317–352.

(39) Hammonds, K. D.; McDonald, I. R.; Tildesley, D. J. Computational Studies of the Structure of Monolayers of Chlorine Physisorbed on the Basal-Plane of Graphite. *Mol. Phys.* **1993**, *78* (1), 173–189.

(40) Lang, N. D.; Kohn, W. Theory of Metal-Surfaces - Induced Surface Charge and Image Potential. *Phys. Rev. B: Condens. Matter Mater. Phys.* **1973**, *7* (8), 3541–3550.

(41) Peters, G. H.; Velasco, E. Influence of Surface and Torsion Potentials on the Melting Properties of a Hexane Monolayer on a Graphite Substrate a Molecular-Dynamics Simulation Study. *Mol. Phys.* **1995**, *84* (5), 1039–1047.

(42) Schlick, T.; Fogelson, A. Tnpack - a Truncated Newton Minimization Package for Large-Scale Problems 0.1. Algorithm and Usage. *ACM Trans. Math. Software* **1992**, *18* (1), 46–70.

(43) Martyna, G. J.; Klein, M. L.; Tuckerman, M. Nose-Hoover Chains—the Canonical Ensemble Via Continuous Dynamics. *J. Chem. Phys.* **1992**, *97* (4), 2635–2643.

(44) Nose, S. A Unified Formulation of the Constant Temperature Molecular-Dynamics Methods. *J. Chem. Phys.* **1984**, *81* (1), 511–519.

(45) Parrinello, M.; Rahman, A. Polymorphic Transitions in Single-Crystals—a New Molecular-Dynamics Method. *J. Appl. Phys.* **1981**, *52* (12), 7182–7190.

(46) Liang, W.; Whangbo, M. H.; Wawukschewski, A.; Cantow, H. J.; Magonov, S. N. Electronic Origin of Scanning-Tunneling-Microscopy Images and Carbon Skeleton Orientations of Normal-Alkanes Adsorbed on Graphite. *Adv. Mater.* **1993**, *5* (11), 817–821.

(47) Groszek, A. J. Selective Adsorption at Graphite/Hydrocarbon Interfaces. *Proc. R. Soc. London, A* **1970**, *314* (1519), 473–498.

(48) Magonov, S. N.; Yerina, N. A. High-temperature atomic force microscopy of normal alkane C₆₀H₁₂₂ films on graphite. *Langmuir* **2003**, *19* (3), 500–504.

(49) Cincotti, S.; Rabe, J. P. Self-Assembled Alkane Monolayers on MoS₂ and Mos2. *Appl. Phys. Lett.* **1993**, *62* (26), 3531–3533.

(50) Li, Y. H.; Krilov, G.; Berne, B. J. Elastic bag model for molecular dynamics simulations of solvated systems: Application to liquid water and solvated peptides. *J. Phys. Chem. B* **2006**, *110* (26), 13256–13263.

(51) Watel, G.; Thibaudau, F.; Cousty, J. Direct Observation of Long-Chain Alkane Bilayer Films on Graphite by Scanning Tunneling Microscopy. *Surf. Sci. Lett.* **1993**, *281* (1–2), L297–L302.

(52) Herwig, K. W.; Matthies, B.; Taub, H. Solvent Effects on the Monolayer Structure of Long *n*-Alkane Molecules Adsorbed on Graphite. *Phys. Rev. Lett.* **1995**, *75* (17), 3154.

(53) Khandkar, M. D.; Balasubramanian, S. Argon multilayers on a corrugated surface: effect of coverage on structure. *Chem. Phys. Lett.* **2002**, *362* (1–2), 144–150.

(54) Claypool, C. L.; Faglioni, F.; Goddard, W. A.; Lewis, N. S. Tunneling mechanism implications from an STM study of H₃C(CH₂)₁₅HC=C=CH(CH₂)₁₅CH₃ on graphite and C₁₄H₂₉OH on MoS₂. *J. Phys. Chem. B* **1999**, *103* (34), 7077–7080.

JP809218R